scientific reports

Check for updates

OPEN

Theory and simulation of far field diffraction patterns in Talbot-based transient grating spectroscopy at X-ray free electron lasers

Andrii Goloborodko[1,2], Carles Serrat[3]✉ & Cristian Svetina[4,5]

The recent extension of transient grating (TG) spectroscopy to the X-ray regime at X-ray free electron lasers (XFEL) facilities has opened new possibilities for studying ultrafast dynamics and nanoscale transport. Recent experiments have employed the Talbot effect to generate excitation gratings in the hard X-rays, e.g., at 7 keV, using X-ray phase masks, enabling simplified, collinear TG setups with only two beams. Despite promising experimental progress, a comprehensive theoretical framework for understanding far-field diffraction patterns in Talbot-based X-ray TG is still lacking. In this work, we present a detailed theoretical study of stationary far-field diffraction patterns in TG spectroscopy using the Talbot effect, providing essential insights for interpreting and optimizing recent XFEL experiments. We systematically investigate: (1) the influence of the sample material properties such as, index of refraction and thickness, and beam intensity, included in the phase effectivity parameter causing broadening of the spatial spectrum; (2) the role of wavefront curvature in modulating diffraction regimes; (3) the effect of sample position on far-field patterns; (4) the emergence of heterodyne effects due to phase shifts across diffraction orders; and (5) the impact of using two different wavelengths for pump and probe beams and analyzing the effect of their relative intensities. Our analysis focuses on static spatial properties rather than dynamical transients, offering a foundation for precise material characterization and nonlinear spectroscopy. Simulations are performed using parameter values representative of XFEL conditions, including hard X-ray wavelengths and sub-micrometer grating periods. The results highlight how phase effectivity, beam parameters, and sample placement govern the formation of non-trivial diffraction patterns, providing critical guidance for future X-ray TG experiments. The model focuses on nonlinear phase effects at hard X-ray energies, which are generally very weak and become relevant only at high intensities. This study delivers the first systematic theoretical framework for Talbot-based TG spectroscopy, bridging a vital gap in understanding far-field diffraction effects in cutting-edge XFEL applications.

Keywords Transient grating spectroscopy, X-ray free electron lasers, Talbot effect, Far-field diffraction patterns, Heterodyne detection, Nonlinear X-ray wave-mixing

Transient grating (TG) spectroscopy is a time-resolved technique that belongs to the broader family of nonlinear four-wave mixing methods. It is best understood as the time-domain analogue of degenerate four-wave mixing (DFWM), its frequency-domain counterpart[1]. While both techniques rely on the coherent interaction of multiple beams, they differ fundamentally in the nature of the response they generate: TG induces a spatially periodic modulation in the sample, whereas DFWM typically probes a third-order polarization that does not necessarily correspond to a real-space structure. Crucially, TG does not require the emission of a four-wave mixing signal. Its response may result from any photoinduced change in the material–be it absorption, refractive index (including Kerr-type effects), or other properties. In contrast to DFWM, which relies on temporal overlap or long-lived coherence, TG signals can be observed well after excitation and are fully compatible with incoherent or diffusive processes such as thermal relaxation or carrier transport.

[1]PWGP Labs, 14 Zabaryla Str., Bucha, Ukraine. [2]Tieto Poland Sp.Z.O.O., 30 Piastow Al., Szczecin, Poland. [3]Department of Physics, Universitat Politècnica de Catalunya, R. S. Nebridi 22, 08222 Terrassa, Spain. [4]Madrid Institute for Advanced Studies, IMDEA Nanociencia, Calle Faraday 9, Ciudad Universitaria de Cantoblanco, 28049 Madrid, Spain. [5]European XFEL, Holzkoppel 4, 22869 Schenefeld, Germany. ✉email: carles.serrat-jurado@upc.edu

In TG, the interference of two pump pulses creates an excitation grating with periodicity $\Lambda = \lambda/2\sin(\theta)$, corresponding to a momentum transfer $q = 2\pi/\Lambda$. By varying the beams' crossing angle or wavelength, the grating pitch–and thus the momentum exchanged with the system–can be precisely controlled. The excitation grating transfers energy into the system and transiently modifies the refractive index. This variation can be detected by impinging a time-delayed third beam (the probe) onto the grating. The resulting diffraction signal is emitted in a specific direction that fulfills energy and momentum conservation – formally analogous to the phase-matching condition in DFWM. Temporal delays from femtoseconds up to seconds can be accessed, making TG a powerful technique capable of probing dynamics spanning, in principle, over 15 orders of magnitude, with exceptional signal-to-noise ratio[2]. With the aid of a replica of the probe beam (called the local oscillator), spatially and temporally overlapped with the signal, heterodyne detection becomes possible. This technique enables disentangling the amplitude and phase components of the signal, allowing access to the real and imaginary parts of the dielectric function. Heterodyne detection also linearizes the signal with respect to the material's response, amplifies it, and significantly improves the signal-to-noise ratio by orders of magnitude[3].

Optical TG was developed in the 1970s and 1980s and was primarily used in physical chemistry to study molecular vibrations, phonon dynamics, and energy transfer processes[1,4–9]. More recently, its applications have expanded to fields such as thermal transport, ultrafast magnetism, and nanoscale energy transfer[10–12]. TG is commonly used to probe transport processes in matter and quasi-particle dynamics. The flexibility of TG makes it an invaluable tool for materials science. By adjusting the incident angle of the pump pulses, the spatial period of the grating can be tuned, enabling the study of transport phenomena across multiple length scales. For instance, thermal grating formation enables the direct measurement of in-plane heat transport, crucial for the development of thermally anisotropic materials and nanostructures. Moreover, the polarization of the pump beams can play a significant role in generating amplitude versus polarization gratings, which can be utilized to study chiral and magnetic systems[13,14]. Additionally, TG has shown promise in probing surface acoustic waves and thermal waves in various material systems, revealing key insights into nanoscale transport dynamics.

Optical wavelengths employed in TG, however, limit the reachable spatial resolution and do not generally provide chemical specificity. These limitations can be overcome by employing shorter wavelengths, e.g., high photon energies such as Extreme Ultraviolet (EUV), soft, and hard X-rays. The advent of X-ray free-electron lasers (XFELs) has opened a new era for ultrafast science, enabling time-resolved measurements of molecular dynamics, the exploration of material properties under extreme conditions, and single-particle scattering imaging[15]. XFELs provide tunable multi-color[16] ultrashort pulses (down to the attosecond)[17] with polarization control and intensities up to several millijoules, effectively functioning as high photon energy lasers. Thanks to XFELs, TG was extended to the EUV range at FERMI[18–21], and a dedicated instrument is now routinely used for TG experiments, reaching tens of nanometer spatial resolution and accessing some element resonances[22]. EUV-TG is a consolidated methodology that allows the study of transport in condensed matter systems at the mesoscale with ultrafast time resolution. Extension of TG to X-rays would allow single-digit nanometer spatial resolution and include K, L, and M shells of many elements in biological systems and current technologies such as oxygen, nitrogen, carbon, iron, rare earths, and lanthanides. As of today, X-ray TG is challenging and still under development. One of the main challenges in performing X-ray transient grating experiments is the transport, control, and manipulation of X-rays: mirrors typically operate at grazing incidence unless special multilayer coatings are employed, and while moderate vacuum conditions may suffice for short distances, ultra-high vacuum is generally required over longer beamlines to minimize absorption and preserve beam quality. Moreover, TG setups involving multiple overlapping beams and phase masks demand stringent alignment and spatial resolution, further increasing experimental complexity[23,24].

To overcome these difficulties, we have proposed exploiting the Talbot effect to generate the TG excitation grating in X-rays using a phase mask, i.e., a periodic object capable of diffracting X-rays into several orders. The Talbot effect was already applied to TG in the optical range[25] and, with a collimated pump-probe geometry, has proven capable of providing heterodyne detection. Application of the Talbot effect to TG enables the use of only two pulses instead of three (the pumps are generated by the phase mask), allowing also to work in collinear geometry, thus simplifying the experimental setup. Recent implementations of this concept have proven the feasibility of generating TG excitation[26], performing X-ray TG pump - optical probe spectroscopy[27,28], and more recently, all X-ray TG employing X-rays for both pump and probe[29]. These findings open the new field of X-ray TG and hold the promise of studying transport at the nanoscale. Despite these experimental advances, until now, there has been no dedicated study exploring the application of the Talbot effect to TG under realistic experimental conditions, such as high photon energy, sub-micrometer TG pitches, and the presence of pump and probe beams. In this work, we investigate far-field diffraction effects in a TG configuration that employs the Talbot effect, similar to approaches used in recent XFEL experiments.

We investigate the far-field characteristics of TG spectroscopy by analyzing the stationary diffraction patterns formed under various experimental conditions. Specifically, we examine the influence of phase effectiveness and beam intensity, wavefront curvature, and sample position on the diffraction patterns, considering a single input beam. We further investigate the heterodyne effect in the diffraction pattern by employing a self-diffraction geometry, focusing on how phase shifts across different diffraction orders introduce specific spatial frequencies that enhance the characterization of grating-to-sample distances. These dependencies provide an additional layer for interpreting material responses, particularly through spatial frequencies unique to the heterodyne signal. We then study the effect of introducing a second beam with a different wavelength in a pump-probe scenario and evaluate how the ratio between their intensities alters the diffraction outcome in the far field.

The simulations performed in this study utilize parameter values relevant to recent XFEL experiments[29], such as hard X-ray wavelengths and fine grating periods, ensuring that the results are directly applicable to ultrafast spectroscopy setups in these advanced facilities. By utilizing the Talbot effect, our setup differs from traditional transient grating spectroscopy, where crossed beams form the grating. Instead, we use a physical

grating (phase mask) to produce a grating pattern on the sample and analyze the far-field image as a function of realistic parameters. Unlike in crossed-beam geometries, where the excitation grating is fixed in space, the Talbot geometry produces a periodic intensity pattern that evolves along the propagation axis due to near-field diffraction. This spatial evolution allows the sample to be positioned at different planes within the Talbot carpet, offering enhanced flexibility for probing material responses at various spatial phases of the excitation pattern. Moreover, by designing multilayer systems with a periodicity matched to the Talbot longitudinal modulation, it becomes possible to selectively excite specific layers and investigate their dynamics, with the longitudinal spacing tunable through experimental parameters.To isolate the geometric and nonlinear phase contributions to the far-field pattern, we focus on a limiting case where absorption is negligible, as in low-Z materials operated far from resonances. The nonlinear refractive response is also expected to be small under typical XFEL intensities, as discussed in Sec. 2.

The layout of the paper is as follows: Section "Theory and simulations" details the underlying theory of far-field diffraction effects in Talbot-based TG spectroscopy. Additionally, the general properties of far-field pattern formation are characterized, and the effect of the material's nonlinear response together with the input intensities on the diffraction pattern is examined. Section "Results and discussion" presents calculation results for the spatial spectrum's dependence on wavefront curvature and sample position with a single focused Gaussian input beam—i.e., *self-diffraction*, examines heterodyne configurations, and investigates the effect of an additional beam in a pump-probe scheme. A discussion and concluding remarks are provided in Section "Discussion and conclusions".

Theory and simulations

The Talbot effect, first described by H.F. Talbot in 1836[30], is a near-field diffraction phenomenon in which a periodic structure illuminated by coherent light self-replicates its spatial pattern at specific intervals, known as Talbot distances. Our study focuses on the effect of the geometry and the sample response to an excitation grating, enabling the analysis of static spatial properties without involving dynamic processes. Building on the principles of TG geometry in a pump-probe configuration (see Fig. 1), we introduce an effective technique to detect the sequence of Talbot distances, which reflect the spatial parameters of the grating, and reveal the existence of the heterodyne effect.

Throughout this work, the pump and probe beams are diffracted by a transmission phase grating G located in the plane $(\xi, \eta \,|\, 0)$. To clarify the coordinate system used in this study, the following conventions are adopted:

- (ξ, η) represent the in-plane coordinates of the grating G, positioned at $z = 0$.
- (x_0, y_0) denote the coordinates at the sample plane, located at a distance z_0 from the grating.
- (x, y) are the coordinates at the plane of the 2D PSD, placed at a distance Z from the grating.

In order to consistently refer to these coordinate systems in different planes, the notation $(x, y \,|\, z)$ is used, where the symbol "|" separates the transverse (x, y) and longitudinal (z) components in three-dimensional space.

Since both the pump and probe beams, which in what follows will be considered collinear, overlap on the sample, located in the plane $(x_0, y_0 \,|\, z_0)$, a pattern with spatial periodicity dependent on the pump and probe wavelengths is formed on the sample (sample grating). The 2D PSD, situated in the plane $(x, y \,|\, Z)$, records the resulting far-field diffraction pattern produced by the interaction of the beams with the sample grating.

Let us consider that the physical diffraction grating G, with complex transmittance $T(\xi, \eta)$, is illuminated with a Gaussian field with a spherical wavefront:

$$E(\xi, \eta|0) = E_0 G(\xi, \eta) \mathrm{e}^{j\pi\left(\frac{\xi^2+\eta^2}{\lambda R} + \frac{\xi \sin\alpha_x + \eta \sin\alpha_y}{\lambda}\right)}, \tag{1}$$

where E_0 stands for the initial amplitude, R is the wavefront curvature radius, α_x and α_y are the angles between the projections of the pump and probe beams in the $x - z$ and $y - z$ planes, correspondingly, and $G(\xi, \eta)$ is the Gaussian beam representation[31]:

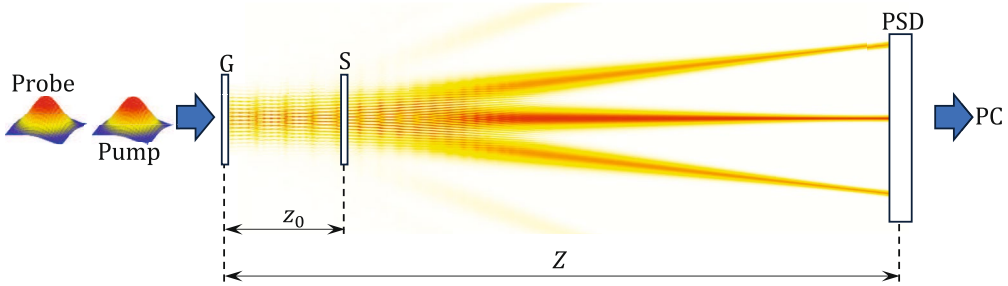

Fig. 1. Schematic diagram of a Talbot-based TG setup. Typically, two beams–a pump and a probe–illuminate the grating (G), which is positioned before the sample (S). The far-field diffraction pattern is recorded by a two-dimensional (2D) position-sensitive detector (PSD). Note that the Talbot carpet shown is generated only by the pump.

$$G(\xi,\eta) = \mathrm{e}^{-\frac{\xi^2+\eta^2}{2a^2}} \mathrm{e}^{j\psi_0 \frac{R_0^2}{\xi^2+\eta^2+R_0^2}}, \tag{2}$$

where a is the beam radius or waist value, R_0 and ψ_0 are the Hermite-Gaussian beam phase parameters[32]. In what follows, we assume that $R_0 = \infty$, and since intensity is the detection value, we neglect the constant phase coefficient ψ_0 ($\psi_0 = 0$). Now suppose that the grating transmittance $T(\xi,\eta)$ can be mathematically represented in terms of a Fourier series[33]:

$$T(\xi,\eta) = T_0 \sum_{n,m} C_{n,m} \mathrm{e}^{j\frac{2\pi}{\Lambda_x} n\xi + \frac{2\pi}{\Lambda_y} m\eta}, \tag{3}$$

where T_0 represents the mean transmittance function for an infinite grating, Λ_x and Λ_y are the spatial periods of the grating along the x and y axes, and $\{C_{n,m}\}$ are the Fourier coefficients associated with the grating unit cell[34]. At the distance z_0 from the grating G, the amplitude distribution of the optical field is expressed as[35]:

$$E(x_0,y_0|z_0) = T_0 \frac{\mathrm{e}^{j2\pi\frac{z_0}{\lambda}}}{j\lambda z_0} \sum_{n,m} C_{n,m} \iint_{-\infty}^{+\infty} E(\xi,\eta|0) \mathrm{e}^{j\frac{2\pi}{\Lambda_x} n\xi + \frac{2\pi}{\Lambda_y} m\eta + j\pi\frac{(x_0-\xi)^2+(y_0-\eta)^2}{\lambda z_0}} \mathrm{d}\xi\mathrm{d}\eta. \tag{4}$$

We factorize the Fourier coefficients as $C_{n,m} = C_n C_m$ based on the assumption that the grating's transmittance function is separable along the x- and y-axes. This allows the grating to be modeled as the product of two independent 1D periodic functions. Therefore, Eq. (4) can be rewritten as:

$$E(x_0,y_0|z_0) = E_0 T_0 \mathrm{e}^{j2\pi\frac{z_0}{\lambda}} \frac{1}{j\lambda z_0} E(x_0|z_0) E(y_0|z_0), \tag{5}$$

where the amplitudes $E(x_0|z_0)$ and $E(y_0|z_0)$ are defined as:

$$\begin{aligned} E(x_0|z_0) &= \sum_n C_n \int_{-\infty}^{+\infty} \mathrm{e}^{-\frac{\xi^2}{2a^2} + j\frac{2\pi}{\Lambda_x} n\xi + j\pi\frac{(x_0-\xi)^2}{\lambda z_0} + j\pi\left(\frac{\xi^2}{\lambda R} + \frac{\xi}{\lambda}\sin\alpha_x\right)} \mathrm{d}\xi \\ &= \mathrm{e}^{j\pi\frac{x_0^2}{\lambda z_0}} \sqrt{\frac{\pi 2a^2\lambda z_0 R}{\lambda z_0 R + 2a^2 j\pi(R+z_0)}} \sum_n C_n \mathrm{e}^{-\pi^2\left(\frac{n}{\Lambda_x} - \frac{x_0}{\lambda z_0} + \frac{1}{2\lambda}\sin\alpha_x\right)^2 \frac{2a^2\lambda z_0 R}{\lambda z_0 R + 2a^2 j\pi(R+z_0)}}. \end{aligned} \tag{6}$$

One should note that for the y-axis, the field distribution is represented in the same manner but with different period and coordinate values.

In our model, the sample transmittance accounts for the nonlinear phase shift induced by the Kerr effect. We specifically consider a sample material exhibiting the Kerr effect while neglecting absorption and scattering losses. Under this assumption, the intensity-dependent refractive index n is given by[36,37]:

$$n(x_0,z_0) = n_0 + \Delta n(x_0,z_0) = n_0 + n_2 I(x_0,z_0), \tag{7}$$

where n_0 is the linear refractive index, n_2 is the nonlinear refractive index coefficient, and $I(x_0,z_0)$ denotes the local intensity distribution. In the X-ray and hard X-ray regimes, neglecting losses is generally a valid approximation for low-Z materials with minimal absorption, such e.g. diamond, when operating far from absorption edges or resonances. In this regime, the nonlinear refractive index n_2 becomes very small due to the weak electronic response at high photon energies, resulting in minimal dispersion and absorption and an almost negligible wavelength dependence of n_2. However, under high-intensity irradiation, nonlinear absorption processes, such as multiphoton ionization and free carrier generation, can introduce significant losses. These effects limit the present model's applicability in extreme conditions or in materials with inherent absorption, as the absence of resonant enhancement leads to a stable but weak nonlinear optical response across the spectrum. We emphasize that the model is constructed as a limiting case to isolate the role of nonlinear phase modulation in the absence of absorption-driven amplitude changes. Nonetheless, extending the model to include absorption is straightforward: linear losses can be incorporated via a complex refractive index $n = n' + j\kappa$, and nonlinear absorption mechanisms may also be included to improve accuracy under more general conditions. The amplitude modulation of the transient grating (TG) signal affects the far-field pattern over a much narrower angular range than phase or frequency modulation[38], since phase modulation results in a significantly broader spatial frequency spectrum[39]. Although the diffraction angles themselves are determined by geometry and thus identical for both types of modulation, the spatial frequency content and energy distribution across diffraction orders differ. Pure phase gratings tend to generate a richer spectrum of higher-order diffraction components, whereas amplitude gratings primarily redistribute intensity between the zeroth and first orders. This difference arises because phase modulation introduces rapid spatial phase variations without attenuating the beam, effectively acting as a higher-order Fourier mask. Therefore, the simplification adopted in our model—considering only phase effects linked to the real part of the complex refractive index—is intrinsically limited, as it neglects some low-order diffraction processes. On the other hand, if a nonlinear effect manifests even under purely phase modulation, its signature would likely be even more pronounced when amplitude effects are included, which typically enhance ± 1 diffraction orders.

Note that since both the pump and probe beams pass through a physical grating (G) (see Fig. 1), the resulting pattern on the sample has a period that depends on the pump (λ_0) and probe (λ_1) wavelengths. The light intensity on the sample is given by:

$$I\left(x_0 \mid z_0\right) = I_{\lambda_0}\left(x_0 \mid z_0\right) + I_{\lambda_1}\left(x_0 \mid z_0\right), \tag{8}$$

where $I_{\lambda_0}\left(x_0 \mid z_0\right)$ and $I_{\lambda_1}\left(x_0 \mid z_0\right)$ represent the pump and probe beam intensities, respectively, defined as:

$$I_{\lambda}\left(x_0 \mid z_0\right) = E_{\lambda}\left(x_0 \mid z_0\right) E_{\lambda}^{*}\left(x_0 \mid z_0\right), \tag{9}$$

where the symbol * denotes complex conjugation and λ refers to both the pump (λ_0) and probe (λ_1) wavelengths. Consequently, the phase shift induced by the sample on the probe with wavelength λ_1 is expressed as:

$$\Phi\left(x_0|z_0\right) = \Phi_0 + \Delta\Phi\left(x_0|z_0\right) = 2\pi\frac{s}{\lambda_1}n_0 + 2\pi\frac{s}{\lambda_1}n_2 I\left(x_0 \mid z_0\right), \tag{10}$$

where s is the sample thickness. As a result, the transmittance function for the grating on the sample can be expressed as:

$$T_T\left(x_0|z_0\right) \sim \mathrm{e}^{j2\pi\frac{s}{\lambda_1}n_2 I(x_0|z_0)}, \tag{11}$$

where the constant multiplier is neglected since intensity is the observable quantity. Note that the coordinate-dependent part of the phase shift in Eq. (10) depends on the sample thickness s, the wavelength λ_1, and the beam intensity in Eq. (9). This dependence can be conveniently expressed by introducing a single parameter β, which combines the effective phase shift $2\pi\frac{s}{\lambda_1}n_2$ and the sum of the peak intensities of the two beams $I_0 = I_{0\lambda_0} + I_{0\lambda_1}$:

$$\beta = 2\pi\frac{s}{\lambda_1}n_2 I_0. \tag{12}$$

Therefore, the sample transmittance (11) will be represented as:

$$T_T\left(x_0|z_0\right) \sim \mathrm{e}^{j\beta I_{\beta}(x_0|z_0)}, \tag{13}$$

where $I_{\beta}\left(x_0 \mid z_0\right)$ is the normalized intensity on the sample:

$$I_{\beta}\left(x_0 \mid z_0\right) = I\left(x_0|z_0\right) I_0^{-1} \quad \text{where} \quad 0 \le I_{\beta}\left(x_0 \mid z_0\right) \le 1. \tag{14}$$

All subsequent analysis will be carried out using the *phase effectivity* parameter β, which characterizes the sample material through its nonlinear refractive index n_2 and thickness *s*, and accounts for the intensities of the input beams I_0.

Note, that finite grating transmittance $T_T\left(x_0|z_0\right)$ can be represented via its spatial spectrum[40]:

$$S\left(f|z_0\right) = \int_{-\infty}^{+\infty} T_T\left(x_0|z_0\right) \mathrm{e}^{-j2\pi f x_0}\mathrm{d}x_0, \tag{15}$$

where *f* stands for the spatial frequency. This allows the Fresnel integral to be expressed as a sum of spatial harmonics. Therefore, taking into account the form of Eq. (15), the field distribution on the 2D PSD can be represented as:

$$E(x, y|Z, z_0) = E_0 T_0 \frac{\mathrm{e}^{j2\pi\frac{Z}{\lambda}}}{\lambda z_0(z_0 - Z)} E(x|Z, z_0) E(y|Z, z_0), \tag{16}$$

where the amplitude $E(x|Z, z_0)$ is defined as:

$$\begin{aligned} E(x|Z, z_0) &= \sum_n C_n \iiint_{-\infty}^{+\infty} S\left(f|z_0\right) \mathrm{e}^{-\frac{\xi^2}{2a^2} + j\frac{2\pi}{\Lambda_x}n\xi + j\pi\frac{(x_0-\xi)^2}{\lambda z_0} + j\pi\left(\frac{\xi^2}{\lambda R} + \frac{\xi}{\lambda}\sin\alpha_x + 2f x_0 + \frac{(x-x_0)^2}{\lambda(Z-z_0)}\right)} \mathrm{d}\xi\mathrm{d}x_0\mathrm{d}f \\ &= \sqrt{\frac{2\pi a^2\lambda RZ}{RZ\lambda + j2\pi a^2(R+Z)}} \sum_n C_n \int_{-\infty}^{+\infty} S\left(f|z_0\right) \mathrm{e}^{-\pi^2\left(\frac{n}{\Lambda_x} - \frac{x}{\lambda z_0} + \frac{1}{2\lambda}\sin\alpha_x + f\frac{Z-z_0}{Z}\right)^2 \frac{2a^2\lambda ZR}{\lambda ZR + 2a^2 j\pi(R+Z)}} \\ &\quad \times \mathrm{e}^{j\pi\frac{(Z-z_0)z_0}{Z}\lambda\left(\frac{x}{\lambda(Z-z_0)} - f\right)^2} \mathrm{d}f. \end{aligned} \tag{17}$$

The expression for $E(y|Z, z_0)$ is analogous to Eq. (17), with the substitutions $x \to y$, $\Lambda_x \to \Lambda_y$, and $\alpha_x \to \alpha_y$. One can see that if the phase effectivity β is zero, i.e. for a purely linear behavior of the sample, only one spatial

frequency - which is equal to zero, is present in the spatial spectrum $S(f|z_0)$. Thus, Eq. (17) reduces to Eq. (6) with a different distance parameter.

To assess the expected strength of the nonlinear phase modulation, we estimate the maximum phase shift $\Delta\Phi$ induced by the Kerr effect under realistic XFEL conditions. For a material with nonlinear index n_2, the phase shift experienced by the probe beam after traversing a sample of thickness s with peak intensity I is:

$$\Delta\Phi = \frac{2\pi s}{\lambda} n_2 I. \tag{18}$$

Using representative values $\lambda = 0.17\,\mathrm{nm}$ (7.3 keV) and an estimated $n_2 \sim 10^{-24}\,\mathrm{m^2/W}$ for diamond in the hard X-ray regime, the intensity required to induce a nonlinear phase shift $\Delta\Phi \sim 1$ is approximately $3 \times 10^{15}\,\mathrm{W/cm^2}$ for a sample thickness $s = 1\,\mu\mathrm{m}$. For thicker samples, such as $s = 10\,\mu\mathrm{m}$, a value routinely used in XFEL experiments, the required intensity drops by an order of magnitude to $\sim 3 \times 10^{14}\,\mathrm{W/cm^2}$. This brings the present model within reach of high-intensity XFEL-based experiments. The chosen value of n_2 reflects a conservative extrapolation from optical measurements in diamond [41], where n_2 reaches $\sim 10^{-19}\,\mathrm{m^2/W}$. A reduction by five orders of magnitude is consistent with the expected suppression of the dispersive Kerr response at X-ray frequencies, where electrons cannot follow the fast field oscillations. This interpretation aligns with experimental observations of nonlinear X-ray processes such as two-photon absorption [42], which predominantly probe the absorptive rather than the refractive component of the nonlinear susceptibility.

Far-field pattern formation

In this subsection, the formation of the far-field diffraction pattern is analyzed under two conditions: (1) when the grating is illuminated by a Gaussian beam with a plane wavefront ($R = \infty$) at different incidence angles, where the sample grating's spatial period Λ matches that of the original grating, and the system's spatial spectrum is primarily influenced by the grating shift angle α_x [43]; and (2) when the grating is illuminated by a convergent or divergent Gaussian beam, where the sample grating's spatial period varies depending on the Talbot plane number[44,45].

It should be noted that for a certain region near the focus, the different diffraction orders cease to interfere. This region depends on the beam waist a and the wavefront curvature radius R[46,47]. The following discussion focuses on how these parameters affect the far-field pattern's spatial distribution and shifts.

For a plane Gaussian beam, Eq. (17) reduces to:

$$E(x|Z,z_0) = \sqrt{\frac{2\pi a^2 \lambda Z}{Z\lambda + j2\pi a^2}} \sum_n C_n \int_{-\infty}^{+\infty} S(f|z_0)\, \mathrm{e}^{-\pi^2 \left(\frac{n}{\Lambda_x} - \frac{x}{\lambda z_0} + \frac{1}{2\lambda}\sin\alpha_x + f\frac{Z-z_0}{Z}\right)^2 \frac{2a^2\lambda Z}{\lambda Z + 2a^2 j\pi} + j\pi \frac{(Z-z_0)z_0}{Z}\lambda\left(\frac{x}{\lambda(Z-z_0)} - f\right)^2} \mathrm{d}f. \tag{19}$$

This equation shows that the pattern shift in the x-direction is given by $\left|\frac{\pi a^2 Z}{\lambda Z + 2a^2 j\pi}\sin\alpha_x\right|$, and the spatial distribution is influenced by the phase grating G and sample grating shift $\left|f\frac{\pi a^2 z_0}{\lambda Z + 2a^2 j\pi}\sin\alpha_x\right|$.

For a convergent Gaussian beam, the spatial period of the sample grating decreases according to $\Lambda(z) \sim \Lambda(z+R)/|R|$ with $R < 0$ [48]. At a specific propagation distance, the diffraction orders cease to interfere, a condition determined by the wavefront curvature radius [46] (see Fig. 2). This behavior can be categorized into three distinct diffraction regimes: (i) the Fresnel diffraction regime, and (ii) and (iii) the Fraunhofer diffraction regimes. The distinction between regimes (ii) and (iii) arises from the wavefront curvature, which can introduce fine structures in the far-field diffraction pattern due to the interference between different diffraction orders. The transition between the Fresnel (i) and Fraunhofer (ii) regimes depends primarily on the beam waist a, while the transition from Fraunhofer regime (ii) to regime (iii) is influenced by the radius of beam curvature R in conjunction with the phase effectivity β, which governs the spatial spectrum $S(f|z_0)$. As illustrated in Fig. 2, there exists a characteristic distance beyond which different diffraction orders begin to interfere again for convergent finite beams. This distance is given by:

$$z_{(\mathrm{iii})} = \frac{a\Lambda}{2R\sin\theta}, \tag{20}$$

or, using the diffraction angle relation $\sin\theta = \frac{\lambda}{\Lambda}$, it simplifies to:

$$z_{(\mathrm{iii})} = \frac{a\Lambda^2}{2\lambda R}, \tag{21}$$

which can be derived through straightforward geometrical analysis. As mentioned earlier, since β is related to the beam intensity, the boundaries between diffraction regimes also exhibit intensity dependence. However, the influence of the phase effectivity β, and consequently the beam intensity, can be neglected as it contributes only marginally to the value of $z_{(\mathrm{iii})}$.

In contrast, for a divergent Gaussian beam, the spatial period of the sample grating increases relative to the original grating period [46]. Although both convergent and divergent beams eventually reach a region where the diffraction orders cease to interfere, the regime (iii) observed in convergent beams does not occur for divergent beams. In this scenario, the maximum distance for interference-free propagation is defined by:

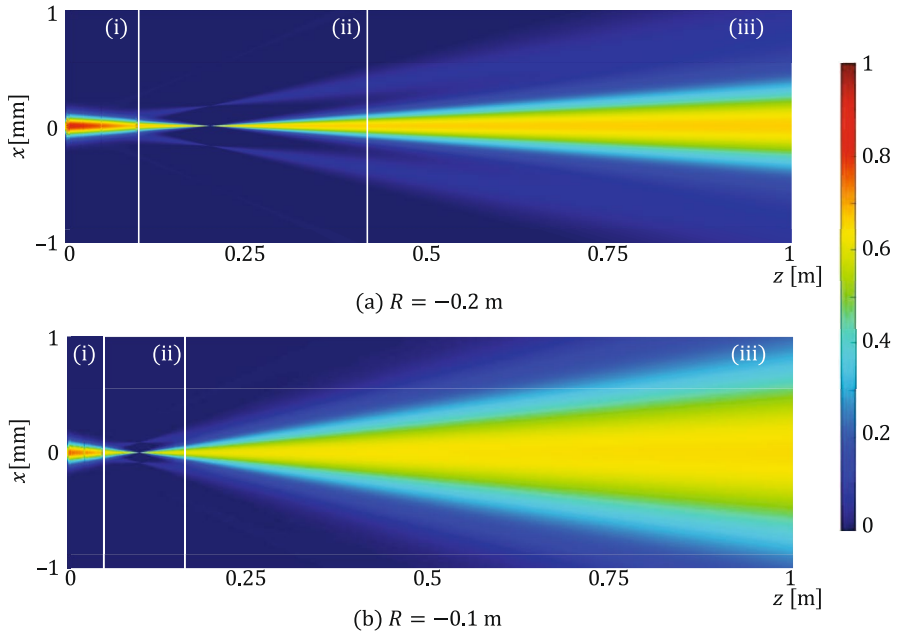

(a) $R = -0.2$ m

(b) $R = -0.1$ m

Fig. 2. Computer-simulated beam contrast in terms of distance z for convergent Gaussian beams with different wavefront curvatures. Simulation parameters are as follows: single input beam (self-diffraction scheme), beam waist $a = 0.1$ mm, grating-to-sample distance $z_0 = 10$ mm, probe wavelength $\lambda = 0.171$ nm, grating period $\Lambda = 0.2$ μm, grating duty factor $d/\Lambda = 0.5$, grating phase depth $\varphi = 0.3$.

$$Z_{\max} = \frac{a}{\Lambda} Z_{\text{eff}}, \tag{22}$$

where the effective Talbot distance is given by:

$$Z_{\text{eff}} = Z_T \frac{\lambda R}{\lambda R + 2\Lambda^2}, \tag{23}$$

and the standard Talbot distance is expressed as:

$$Z_T = 2\frac{\Lambda^2}{\lambda}. \tag{24}$$

This maximum distance, $Z_{\max}$, depends solely on the beam waist a and the grating period Λ [46]. However, if the sample exhibits a nonzero phase effectivity β, $Z_{\max}$ also becomes dependent on the sample grating's spatial spectrum $S(f|z_0)$, introducing additional complexity to the interference behavior.

Far-field pattern characterization

Note that since the sample grating transmittance $T_T(x_0|z_0)$ depends on the field distribution on the sample (see Eqs. (11) and (13)), moving the sample leads to significant changes in the far-field pattern. As the Talbot distance depends on the initial beam radius R and the Talbot plane number for convergent/divergent beams[49], the spatial spectrum at different distances and for varying phase effectivity values changes significantly (see Fig. 3), along with the combination of different grating coefficients $\{C_n\}$ and $S(f|z_0)$ and photon energies.

In Fig. 3, we illustrate a self-diffraction scheme where a single incident beam passes through the grating and undergoes diffraction. In this configuration, the leading edge of the beam interacts with the sample, inducing a periodic modulation in the refractive index. Subsequently, the trailing edge of the same beam diffracts off this induced grating. This self-interference between different temporal segments of the beam effectively eliminates the need for separate pump and probe beams, allowing the observation of nonlinear diffraction effects with a simpler and inherently synchronized setup. To simulate self-diffraction in our theoretical model, we generate the sample grating induced by the pump beam, from which the probe beam diffracts, and we then assume identical intensities and wavelengths for both beams. This configuration establishes the foundation for understanding the more complex pump-probe interaction, which is discussed in detail in Subsection 3.4.

We observe that increasing the phase effectivity value β - which is directly related to the beam intensity on the sample - causes the sample grating spectrum to broaden, resulting in additional intensity peaks appearing in the far-field diffraction pattern. This effect is equivalent to increasing the pattern intensity on the sample, leading to a stronger nonlinear modulation of the refractive index. For the simulations in Fig. 3, a grating with the narrowest spatial spectrum among the tested configurations was used, characterized by a grating duty factor of $d/\Lambda = 0.5$.

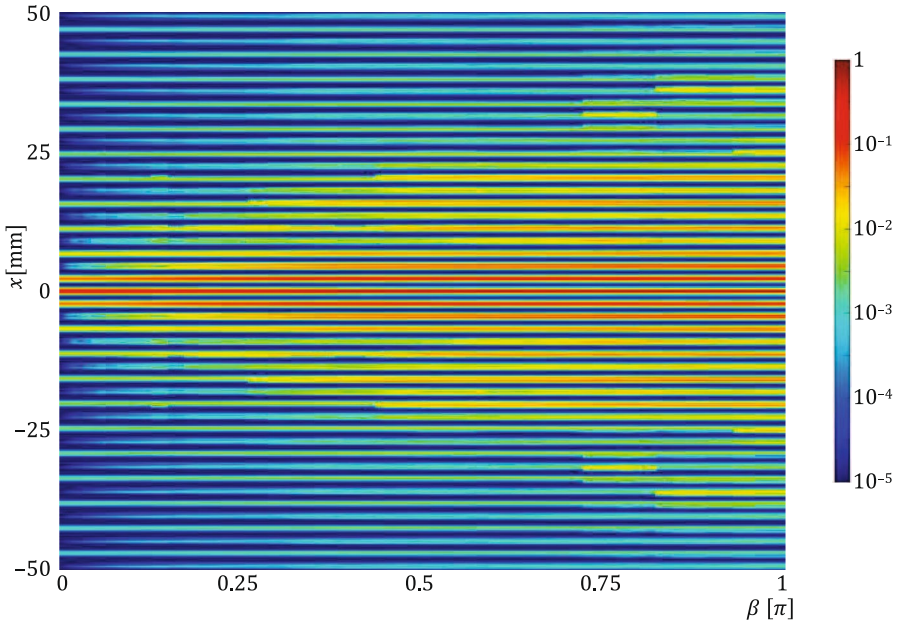

Fig. 3. Far-field pattern dependence for different phase effectivity values. Simulation parameters are as follows: single input beam (self-diffraction scheme), beam waist $a = 0.1$ mm, grating-to-sample distance $z_0 = 10$ mm, sample-to-PSD distance $Z = 2.6$ m, probe wavelength $\lambda = 0.171$ nm, grating period $\Lambda = 0.2$ μm, grating duty factor $d/\Lambda = 0.5$, grating phase depth $\varphi = 0.3$, and wavefront curvature $R = \infty$. These parameter values have been specifically chosen to reflect experimental conditions at XFELs.

The chosen parameters, including the hard X-ray wavelength ($\lambda = 0.171$ nm (7240 eV)) and fine grating period ($\Lambda = 0.2$ μm), are representative of conditions typically encountered in XFEL experiments[29]. It is worth noting that even in the absence of phase effectivity ($\beta = 0$), weak even-order spatial frequencies are inherently present due to the laminar nature of the phase grating, which deviates from an ideal sinusoidal profile. However, even a slight increase in the phase effectivity β significantly enhances these even-order contributions, as evidenced by the more pronounced intensity peaks appearing in the system's spatial spectrum.

Metal plasmonic nanostructures -such as nanowires, nanotubes, and nanoparticles- can also be incorporated into the analysis to explore additional interaction effects. Due to their periodic structure, these metal nanostructures exhibit distinct behavior related to the resonance of surface plasmons, particularly in grooved arrays. Factors such as periodicity, thickness, shape, and size significantly influence the optical response of plasmonic nanostructures. While these parameters are typically known during fabrication, transient grating spectroscopy can offer complementary, non-invasive insight into how such features affect light-matter interaction, particularly under operating conditions or in ultrafast regimes where dynamic optical responses are of interest. Furthermore, X-ray transient grating techniques open unique possibilities for probing ultrafast transport phenomena, such as charge, spin, or heat dynamics, especially in amorphous or liquid systems where conventional imaging methods are inadequate[50,51]. To further investigate how the spatial spectrum in TG configurations depends on these factors, the next section presents several simulations that examine the effects of varying sample distances, pump and probe intensities, and initial wavefront curvatures.

Results and discussion

As demonstrated, the properties of the far-field pattern are influenced by the wavefronts and wavelengths of the pump and probe beams, system distances (z_0 and Z), and beam intensities. To effectively characterize the sample's phase effectivity β, it is advantageous to systematically vary the initial beam curvature, beam intensities, or the grating-to-sample distance. This strategy enables a linear approximation of the phase effectivity β. However, it is equally crucial to identify the optimal parameters that facilitate this estimation while minimizing the associated error. In this section, we examine how these optimal parameters depend on fixed system conditions, which are assumed to align with the experimental setup described in Ref.[29].

The influence of input beam intensities, wavefront curvature, wavelengths, and sample distance has been analyzed through a straightforward computer simulation based on Eq. (17). This simulation involves the following sequential steps: (I) Initialization of the beam, including wavefront curvature and beam radius; (II) Calculation of irradiance in the sample plane; (III) Determination of the spatial spectrum of the sample grating; (IV) Calculation of irradiance in the far-field plane; and (V) Analysis of the resulting far-field patterns.

Wavefront curvature dependence

Figure 4 shows how the far-field pattern depends on the initial wavefront curvature R in the self-diffraction scheme. In this configuration, excitations are caused by a single wavelength, and the spatial frequencies arise

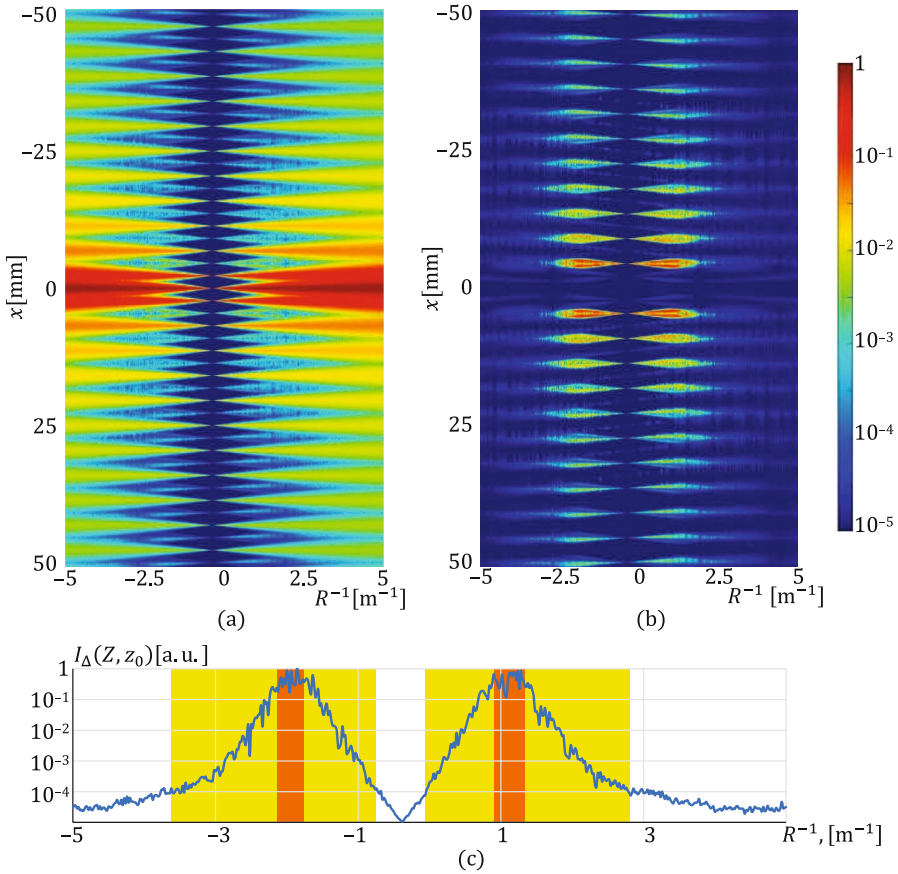

Fig. 4. Far-field pattern dependence for different wavefront curvatures of the Gaussian beam (**a**), difference pattern highlighting the sample effect (**b**), and the integral difference intensity dependence (**c**). Simulation parameters are as follows: single input beam (self-diffraction scheme), beam waist $a = 0.1$ mm, grating-to-sample distance $z_0 = 10$ mm, sample-to-PSD distance $Z = 2.6$ m, probe wavelength $\lambda = 0.171$ nm, grating period $\Lambda = 0.2$ μm, grating duty factor $d/\Lambda = 0.5$, grating phase depth $\varphi = 0.3$, and sample phase effectivity $\beta = 0.1$.

from the Talbot distance of the single input beam. Notably, the minimal pattern pitch values occur for an initial wavefront curvature of $R = -2.61$ m ($R^{-1} \approx 0.4$ m^{-1}), as shown in Fig. 4a. This result is a physical effect and not a numerical artifact. However, the appearance of a zero-intensity region in the figure arises from the simulation resolution: the far-field pattern pitch is 1.5 μm, while the simulation step size is 50 μm. As a result, intensity averaging within this step leads to values approaching zero.

To analyze the sample effect, Fig. 4b shows the differential pattern:

$$I_{\Delta}\left(x|Z, z_0\right) = I_{\beta}\left(x|Z, z_0\right) - I\left(x|Z\right), \tag{25}$$

where $I_{\beta}\left(x|Z, z_0\right)$ is the intensity with the sample having phase effectivity β, and $I\left(x|Z\right)$ is the intensity without the sample. The general pattern difference is calculated as:

$$I_{\Delta}\left(Z, z_0\right) = \frac{1}{A}\int_{-A/2}^{A/2} I_{\Delta}\left(x|Z, z_0\right) \mathrm{d}x, \tag{26}$$

and the dependence is depicted in Fig. 4(c). Figs. 4(a)-(b) are presented in logarithmic scale. The best sensing performance, $I_{\Delta}\left(Z = 2.6 \text{ m}, z_0 = 10 \text{ mm}\right) > 0.2$, is achieved for wavefront curvatures between -2.1 m^{-1} to -1.6 m^{-1} and 0.8 m^{-1} to 1.3 m^{-1}, where the decision threshold of 0.2 is chosen based on a modified Rayleigh criterion.

An alternative optimal sensing range, based on the differences in Figs. 4a,b, spans from -3.4 m^{-1} to -0.7 m^{-1} and from 0 m^{-1} to 2.8 m^{-1}. However, as noted, the Gaussian beam properties depend on the Hermite-Gaussian phase parameter R_0. Here, $R_0 = \infty$, so the optimal measurement range may slightly shift. These regions are considered optimal because they provide the best balance between beam focus and diffraction efficiency. In these zones, the interference between diffraction orders is maximized, leading to enhanced

sensitivity to phase shifts and improved contrast in the far-field diffraction patterns. This enhanced sensitivity facilitates more precise characterization of the sample's nonlinear optical response.

Wavefront curvature can be adjusted in two ways: by moving the grating G while keeping the sample fixed or by moving the grating-sample system together, as considered in this work. Additionally, in an experimental setup, the wavefront curvature can also be tuned by modifying the focusing optics, such as adjusting an X-ray lens or mirror, providing further flexibility in controlling the beam properties. Shifting only the grating (δ_G) changes the grating-to-sample distance z_0, altering the intensity distribution due to variations in the spatial spectrum $S\left(f|z_0\right)$. Conversely, shifting the grating-sample system (δ_{GS}) maintains z_0, resulting in a more stable pattern mainly influenced by β. Fig. 5 illustrates these effects. As shown in Fig. 5b, shifting the entire grating-sample system produces negligible changes in the far-field pattern. Conversely, Fig. 5a exhibits distinct periodic variations in spatial frequencies due to changes in the sample's position. This sensitivity can be systematically analyzed using the Fourier transform:

$$\hat{F}_{I(x|z_0)}(f_Z) = \iint_{-\infty}^{+\infty} E(x|Z,z_0)E^*(x|Z,z_0)\,\mathrm{e}^{-j2\pi f_Z Z}\,\mathrm{d}x\,\mathrm{d}Z, \tag{27}$$

which reveals the field's modal structure as a function of the grating-to-sample distance. The resulting Fourier spectra in Fig. 5c,d display a prominent peak at $0.227\ \mathrm{mm}^{-1}$, corresponding to half of the Talbot distance $Z_T = 0.471$ mm. This feature is absent in Fig. 5b, highlighting the sample position's unique influence on the far-field diffraction pattern. Grating shifts (Fig. 5d) do not introduce Talbot-related spatial frequencies, unlike sample shifts (Fig. 5c), which reveal frequencies around ≈ 0.2 mm, corresponding to the Talbot distance. This analysis of the spatial frequency, directly related to the sample grating and its spectrum $S(f|z_0)$, is crucial for the experimental alignment procedure. It ensures that the sample is accurately positioned in the Talbot plane, where maximum contrast is achieved, and also serves as an indicator of sample-induced effects. Notably, the Talbot distance depends on the initial beam radius R and the Talbot plane number for convergent or divergent

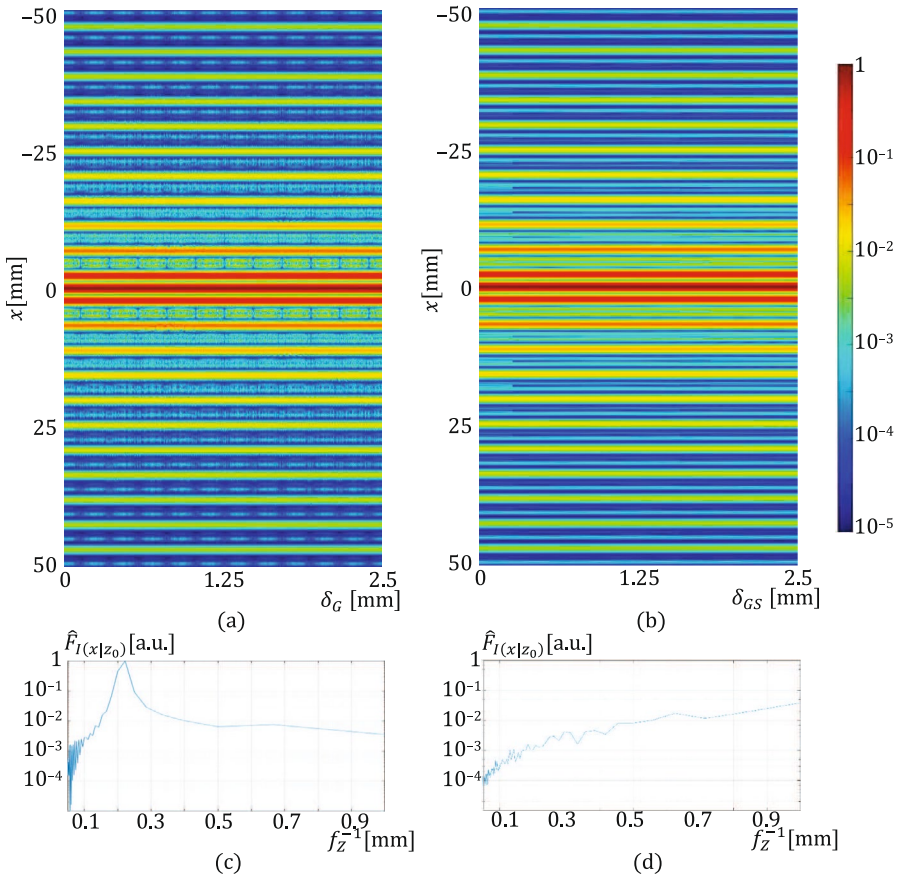

Fig. 5. 1D far-field patterns for different grating (**a**) and grating-sample system (**b**) shifts, together with their spatial spectra (**c**) and (**d**). Simulation parameters: single input beam (self-diffraction scheme is used), beam waist $a = 0.1$ mm, grating-to-sample distance $z_0 = 10$ mm, sample-to-PSD distance $Z = 2.6$ m, probe wavelength $\lambda = 0.171$ nm, grating period $\Lambda = 0.2$ μm, grating duty factor $d/\Lambda = 0.5$, grating phase depth $\varphi = 0.3$, and sample phase effectivity $\beta = 0.1$.

beams. As the scanning range along the z-axis increases, the primary frequency peaks broaden due to evolving spatial coherence.

Sample position dependence

Fig. 6 displays the 1D far-field intensity distribution for various sample-to-grating distances z_0 with a fixed wavefront curvature R.

This spatial frequency, directly linked to the sample grating and its spectrum $S(f|z_0)$, serves as a valuable indicator of sample-induced effects. In this simulation, which assumes a static sample grating without dynamic or time-dependent changes, variations in the spatial frequency primarily reflect the structural properties of the sample and any modifications in the phase grating. Specifically, imperfections, surface roughness, or phase grating variations can introduce measurable shifts or broadening in the spatial frequency components of $S(f|z_0)$. As the scanning range along the z-axis increases, the primary frequency peaks broaden due to evolving spatial coherence, further highlighting the influence of the sample's static structure on the diffraction signal.

Periodic intensity modulations in Fig. 6a arise from intensity variations in the sample plane. The corresponding Talbot carpets, overlaid atop the far-field patterns in Fig. 6, further illustrate this effect. Minima in the far-field pattern coincide with distances where the periodicity in the Talbot image disappears, a consequence of spatial mode redistribution induced by the grating-sample separation[52]. For convergent and divergent Gaussian beams, the Talbot distance is no longer constant and varies with the Talbot plane number[46], contributing to the observed spectral broadening in Fig. 6c,d. To investigate this behavior further, Fig. 7 shows Fourier spectra for two different beam wavelengths in self-diffraction geometry. The spatial frequencies observed are governed by the Talbot distance of the probe beam. As expected, increasing the probe wavelength reduces the Talbot distance, as seen in Fig. 7. Additionally, the spectral decomposition differs for each wavelength: four prominent frequencies are observed for $\lambda = 0.248$ nm, while only two are visible for $\lambda = 0.171$ nm. This difference arises from the intensity distribution's sensitivity to the sample position, shaped by the grating's spatial spectrum $\{C_n\}$, which depends on the duty factor d/Λ. Additionally, since β depends on the nonlinear refractive index n_2, and n_2 is inherently wavelength-dependent, β also varies with the beam wavelength λ (see Eq. (12)). While this

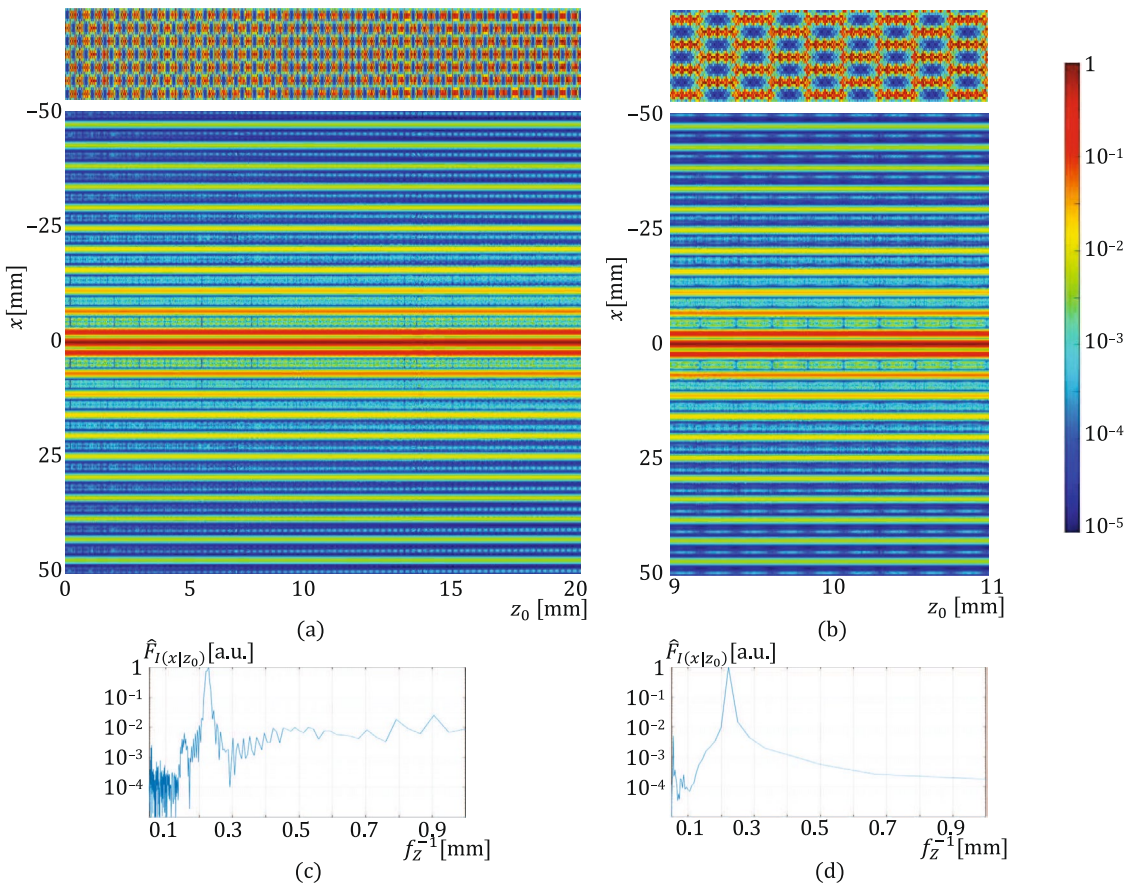

Fig. 6. Far-field pattern dependence for different sample positions and scan distances: 20 mm (**a**) and 2 mm (**b**), with corresponding spatial spectra (**c**) and (**d**). Simulation parameters: single input beam (self-diffraction scheme), beam waist $a = 0.1$ mm, phase grating to detector distance $Z = 2.61$ m, beam wavelength $\lambda = 0.171$ nm, phase grating period $\Lambda = 0.2$ μm, phase grating duty factor $d/\Lambda = 0.5$, phase grating phase depth $\varphi = 0.3$, sample phase effectivity $\beta = 0.1$, and wavefront curvature $R = -550$ mm.

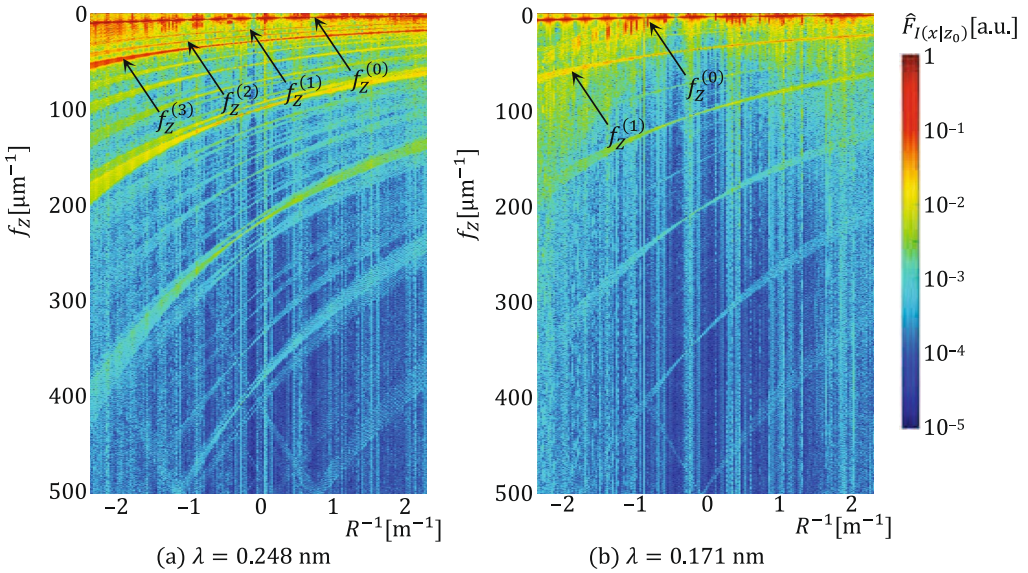

Fig. 7. Spatial frequency dependence on wavefront curvature radius R for two beam wavelengths (self-diffraction scheme). Simulation parameters are: phase grating period $\Lambda = 0.2$ μm, phase grating duty factor $d/\Lambda = 0.5$, phase grating phase depth $\varphi = 0.5$ for $\lambda = 0.248$ nm (**a**) and $\varphi = 0.3$ for $\lambda = 0.171$ nm (**b**), with phase effectivity $\beta = 0.2$.

wavelength dependence becomes more relevant in absorbing samples, such cases are not explicitly considered in the present model but could be readily incorporated.

The Fourier spectra prominently feature the peak $f_Z^{(0)}$, corresponding to half the Talbot length[49]:

$$Z_{T_l} = 2\frac{\Lambda^2 l R}{\lambda R + 2\Lambda^2 l}, \quad l = 1, 2, \ldots \tag{28}$$

This relationship, contingent on the wavefront curvature R, makes the Fourier spectrum a valuable tool for estimating the grating-to-sample distance and the wavelength of the input beam. Furthermore, the grating period, wavefront radius, and grating-to-sample distance collectively dictate the dominant spatial decomposition in any far-field diffraction spectrum. As noted, increasing the scan range broadens the main frequency peak, as observed for $f_Z^{(3)}$ when $1/R < -0.2$ cm^{-1}, or results in frequency mixing, as seen for $f_Z^{(0)}$ and $f_Z^{(1)}$ when $1/R < -0.1$ cm^{-1}. For large scan ranges, this mixing includes higher spatial frequencies associated with Talbot distance variations in divergent beams, resulting in the noisier spectrum observed in Fig. 6c. These components are suppressed in shorter scans, such as in Fig. 6(d), and stem from coherent propagation effects.

Heterodyne effect

Phase shifts across different diffraction orders introduce distinct spatial frequencies into the transient grating's spatial spectrum -a phenomenon known as the heterodyne effect. This effect significantly enhances the interpretative power of far-field diffraction pattern analysis, particularly for precise characterization of the grating-to-sample distance. These phase variations lead to features that are not fully visible in integrated intensity plots, as observed in Fig. 6c,d. Figure 8 illustrates the spatial spectrum across the diffraction aperture for various diffraction orders, based on scans performed at different sample positions shown in Fig. 6b.

According to Ref.[25], the heterodyne signal becomes evident in the first and higher diffraction orders and is characterized by a phase shift ϕ that depends on the grating-to-sample distance z_0:

$$\phi(\theta) = 2\pi\frac{z_0}{\lambda\cos\theta}\left(1 - \cos\theta\right), \tag{29}$$

where θ is the diffraction angle, defined by $\sin\theta = \frac{x}{\sqrt{(Z+z_0)^2+x^2}}$. For small diffraction angles ($x \ll Z + z_0$), Eq. (29) simplifies to:

$$\phi(\theta) \xrightarrow{EMPTY} \phi(x) \approx \pi\frac{z_0}{\lambda(Z+z_0)^2}x^2. \tag{30}$$

This quadratic dependence on x facilitates the identification of heterodyne spatial frequencies, as shown in Fig. 8. In this figure, a set of parabolic lines proportional to $x^2 \sim 0.272(k+1)\left(x\,[\mathrm{mm}] - 2.22\,k\right)^2$ is depicted for diffraction orders $k = 0$ to 3, where darker tones indicate lower diffraction orders. The theoretical coefficient from Eq. (30), $\pi\frac{z_0}{\lambda(Z+z_0)^2} \approx 0.272$ mm^{-2}, aligns well with the observed spatial frequency dependencies,

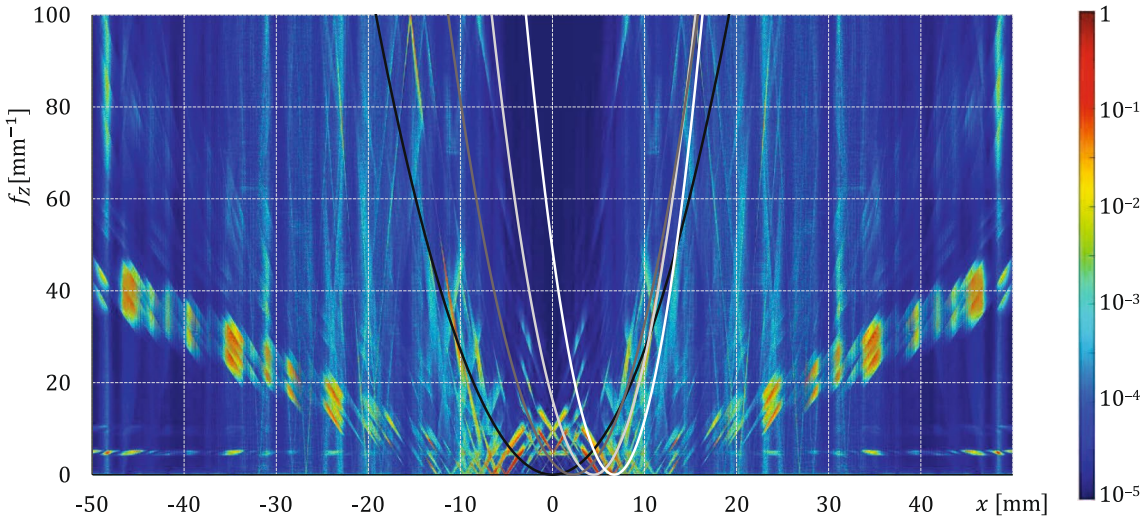

Fig. 8. Spatial frequency distribution across the diffraction aperture; see Fig. 6a.

confirming that the heterodyne signal originates from phase shifts across diffraction orders. The value 2.22 arises from the diffraction order separation constant[53]:

$$\Delta x = \frac{\lambda}{\Lambda}(Z + z_0) \quad \text{with} \quad x_k = k\Delta x. \tag{31}$$

Unlike systems where only a single heterodyne frequency is observed[25], the spatial spectrum here reveals multiple heterodyne frequencies associated with higher diffraction orders. These higher-order phase shifts introduce richer features into the far-field diffraction pattern. While the dominant linear dependence in spatial frequency becomes evident in higher orders, it appears less pronounced due to the beam's intensity distribution, where 95% of the beam energy is confined within -20 to 20 mm. This qualitative analysis highlights the role of the heterodyne effect in introducing order-specific spatial frequencies. However, further quantitative analysis is necessary to fully characterize the dependence of heterodyne frequencies on the diffraction order. Additionally, Talbot-related frequencies are visible in the spatial spectrum, particularly around $f_Z = 5\ \text{mm}^{-1}$ and $f_Z = 10\ \text{mm}^{-1}$, corresponding to spatial periods of 200 μm ($Z_T/2$) and 100 μm ($Z_T/4$), where the Talbot distance $Z_T \approx 470\ \mu$m for the current system configuration. Since a convergent Gaussian beam is used, the Talbot distance is reduced. The coexistence of heterodyne and Talbot-related frequencies in the spatial spectrum provides complementary information about sample positioning and grating phase responses, enriching spatial frequency analysis.

It is also worth noting that these heterodyne frequencies are indeed present in our results. However, as shown in Fig. 8, these frequencies are not constant but vary with the distance from the center of the diffraction pattern (zero diffraction order). In Ref. [25], the heterodyne effect is detected using the zero diffraction order of the probe beam, allowing clearer observation of the heterodyne frequency. In contrast, our analysis integrates the intensity over the $\{-1, 0, +1\}$ diffraction orders. Since the heterodyne frequency depends on the beam's spatial position, this integration effectively averages the contributions of all visible frequencies. As a result, individual heterodyne frequencies are not distinctly resolved in the spatial spectrum but are observed as an overall effect within the frequency distribution.

Equations 29 and 31 are obtained from a geometric analysis of the far-field phase shifts introduced by the relative propagation angles of the probe and diffracted orders. While this treatment is simplified and does not account for wavefront curvature or temporal coherence, it captures the essential spatial phase structure that leads to heterodyne frequency signatures in the diffraction pattern. Regarding signal enhancement, heterodyne detection allows a weak signal field E_{sig} to interfere with a strong local oscillator field E_{LO}, producing an intensity modulation proportional to $2\text{Re}\{E_{\text{sig}}E_{\text{LO}}^*\}$. This linear dependence enables the detection of signals that would otherwise be buried below the noise floor in a direct $|E_{\text{sig}}|^2$ measurement[54]. This enhancement principle is particularly important for X-ray transient grating experiments, where signal levels are extremely low.

In summary, spatial frequencies from the heterodyne effect provide a sensitive method for analyzing grating-to-sample distances. Phase shifts across diffraction orders introduce distinct frequency signatures that enhance material characterization. Beyond its diagnostic role, heterodyne detection amplifies weak nonlinear signals through coherent interference, offering deeper insight into the sample's structural and optical properties. These theoretical predictions invite experimental validation in both optical and X-ray regimes.

Pump-to-probe ratio

This section analyzes the effect of using pump and probe beams with different photon energies and intensities, as in recent XFEL experiments where a phase mask creates two Talbot carpets with distinct periodicities. This dual-wavelength configuration, although experimentally challenging, has been demonstrated using 5 keV and

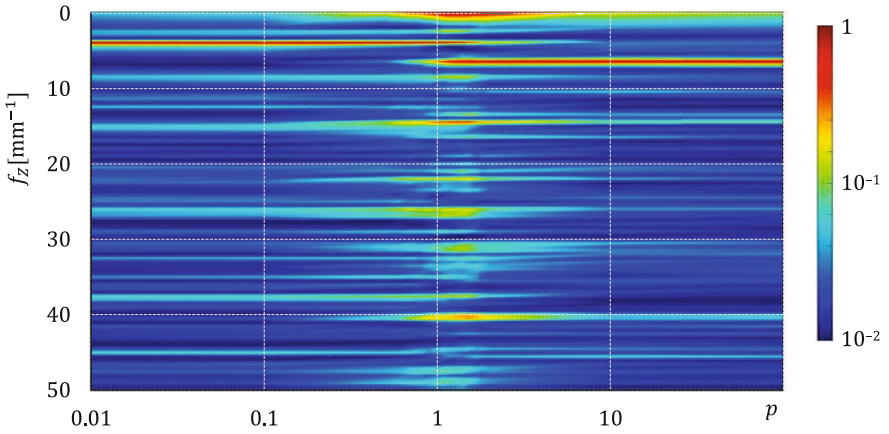

Fig. 9. Spatial frequency distribution for different pump-to-probe intensity ratios p. Simulation parameters: grating period $\Lambda = 0.2$ μm, grating duty factor $d/\Lambda = 0.5$, grating phase depth $\varphi = 0.5$ for $\lambda = 0.248$ nm and $\varphi = 0.3$ for $\lambda = 0.171$ nm, phase effectivity $\beta = 0.1$.

7.2 keV pulses [29], motivating its inclusion in our modeling. Up to this point, we have exclusively considered self-diffraction, where a single beam both generates the grating at the sample and produces the diffraction signal.

Fig. 9 illustrates the impact of introducing two input beams, highlighting how variations in pump and probe intensities affect the configuration with the shifted sample S. The ratio $p = \frac{I_{\lambda_0}}{I_{\lambda_1}}$, where I_{λ_0} and I_{λ_1} are the pump and probe intensities, respectively, is used as the descriptive parameter for this dependency. It is evident that the spatial frequency spectrum can be described as a superposition of the spatial frequencies corresponding to the pump and probe beams when their intensities are equal. Increasing the intensity of one beam makes the spatial frequencies associated with the more intense beam more pronounced.

Notably, when $p < 0.1$ or $p > 10$, the system effectively behaves as if only one dominant beam is present. However, to fully suppress the influence of the weaker beam, a more extreme intensity ratio is required, specifically when $p < 10^{-3}$ or $p > 10^3$. As previously discussed, the far-field diffraction pattern is entirely determined by the intensity distribution on the sample S (see Fig. 1). In the present configuration, where the pump and probe beams have different wavelengths, the resulting spatial frequency distribution becomes more intricate. This complexity arises from the wavelength dependence of the Talbot length, leading to interference effects that cannot be described as a simple superposition of the individual spatial spectra. Consequently, the combined effects of varying both the intensity and wavelength of the input beams play a crucial role in shaping the far-field diffraction patterns, revealing richer and more complex features.

Discussion and conclusions

In this work, we have developed a comprehensive theoretical framework for analyzing stationary far-field diffraction patterns in TG spectroscopy using the Talbot effect. This model directly addresses the growing need for a systematic understanding of recent XFEL experiments[26,27,29], where exploiting the Talbot effect through phase masks simplifies beam manipulation by generating excitation gratings without requiring complex beam configurations. Our findings provide essential insights for designing and interpreting TG experiments in the X-ray regime, particularly under realistic experimental conditions involving high photon energies and sub-micrometer grating periods.

A central result of this study is the role of the phase effectivity parameter, β, a composite quantity that encapsulates the sample's nonlinear refractive index n_2, thickness s, the probe wavelength λ_1, and the beam intensity I_0. Variations in β significantly impact the spatial spectrum of the sample grating: increasing β leads to a broadening of the diffraction pattern and the emergence of additional peaks. This behavior reflects a stronger nonlinear modulation of the refractive index, establishing β as a pivotal factor for tuning the diffraction response and enabling precise material characterization.

Additionally, it is well-established that the wavefront curvature of the input Gaussian beam significantly influences the periodicity of the induced sample grating. Specifically, convergent beams ($R < 0$) compress the grating period, while divergent beams ($R > 0$) expand it [46]. This curvature-induced modulation leads to distinct diffraction regimes, transitioning between Fresnel and Fraunhofer diffraction. In this work, we systematically account for this effect to accurately model the far-field diffraction patterns under varying beam curvatures. Notably, the boundary between these regimes is influenced not only by the beam curvature but also by the phase effectivity β, underscoring the complex interplay between optical geometry and nonlinear material response.

The position of the sample relative to the grating was also identified as a critical factor in shaping the far-field diffraction pattern. Adjusting the sample's position modifies the interference conditions, leading to observable changes in the spatial frequency content of the far-field pattern. Spatial frequencies associated with the Talbot effect and heterodyne interference become more pronounced, providing a powerful tool for precise distance calibration and enhancing sensitivity to the sample's optical properties. Moreover, the heterodyne effect was

investigated, where phase shifts across different diffraction orders introduce distinct spatial frequencies into the far-field diffraction spectrum.

This effect amplifies subtle phase variations in the sample grating, providing an additional layer of sensitivity for probing material responses and enabling more accurate characterization of the grating-to-sample distance. Beyond this, the analysis of heterodyne-induced spatial frequencies offers a powerful diagnostic tool to determine the presence and strength of the heterodyne effect itself. By enabling the extraction of the relative phase between the signal and the local oscillator (reference beam), this approach allows for precise control and manipulation of interference conditions. For the first time in the X-ray regime, this methodology introduces the possibility of exploiting phase-sensitive detection to isolate weak nonlinear signals, resolve fine structural details, and enhance contrast in complex systems. Additionally, controlling the relative spatial alignment in the X, Y, and Z directions provides unprecedented flexibility in tailoring experimental setups for optimized signal detection and material characterization. This advancement paves the way for more sophisticated experimental designs, offering new opportunities to explore ultrafast dynamics and nonlinear phenomena in matter under extreme conditions.

The pump-to-probe intensity ratio was also found to play a critical role in controlling the dominance of spatial frequencies within the diffraction pattern. At balanced intensities, the system exhibits clear dual-beam interference, where the spatial frequency spectrum reflects the combined contributions of both the pump and probe beams. This regime allows for rich interference effects and complex spatial modulations that are sensitive to the relative phase and alignment of the two beams. However, as the intensity ratio becomes extreme, the system gradually transitions to a single-beam regime, where the spatial frequency distribution is dominated by the more intense beam. In this limit, the weaker beam contributes negligibly to the interference pattern, and the diffraction signal effectively reflects only the properties of the dominant beam. This transition highlights the pump-to-probe ratio as a powerful tuning parameter for modulating the system's sensitivity to specific spatial frequency components. By precisely adjusting this ratio, experiments can be designed to either emphasize interference effects for enhanced sensitivity to subtle material responses or suppress them to isolate single-beam diffraction characteristics. This control mechanism is particularly valuable for studying nonlinear optical phenomena, as it enables the selective amplification of desired signals while minimizing background noise. In the context of X-ray experiments, this tunability opens new avenues for phase-sensitive detection and the exploration of ultrafast dynamics in complex materials.

Our simulations were performed using parameters directly relevant to XFEL experiments. These results are immediately applicable to ultrafast spectroscopy setups and provide practical guidelines for optimizing TG experiments aimed at investigating material dynamics with high spatial and temporal resolution. The model highlights the importance of carefully controlling parameters such as phase effectivity, wavefront curvature, and sample position to enhance measurement sensitivity.

Future research should aim to experimentally validate the predictions presented here, with particular focus on heterodyne detection schemes to better resolve phase relationships between signal and reference beams. Extending the model to include time-dependent dynamics and SASE-induced coherence fluctuations will also be essential for understanding ultrafast relaxation and transport phenomena. Finally, exploring more complex grating structures, such as plasmonic or adaptive phase masks, and integrating TG with complementary diagnostics could further expand the technique's applicability to nanoscale material characterization.

In conclusion, this study presents a foundational theoretical model for Talbot-based TG spectroscopy in the X-ray regime. The insights gained are crucial for advancing the design and interpretation of XFEL experiments, enabling precise and high-resolution material characterization. The interplay between phase effectivity, beam geometry, and sample positioning opens new pathways for probing nanoscale dynamics and advancing the capabilities of ultrafast X-ray spectroscopy.

Although the current model neglects absorption, this approximation enables a focused analysis of nonlinear phase effects and their role in diffraction pattern formation. Incorporating absorption and resonance phenomena represents a natural extension, allowing broader applicability under general experimental conditions. Likewise, while the present model describes the stationary spatial diffraction pattern generated by the excitation grating and nonlinear sample response at a fixed pump-probe delay, it does not account for the temporal evolution of the signal. Extending the framework to incorporate explicit time dependence and SASE pulse fluctuations will be essential for fully capturing ultrafast relaxation and transport phenomena, and will be the subject of future work.

Data availability

The datasets generated and analyzed during this study are not publicly accessible due to the extensive number of simulations performed under varied conditions for input beams and optical configurations. However, they can be obtained from the corresponding author upon reasonable request.

Received: 17 January 2025; Accepted: 10 July 2025
Published online: 25 July 2025

References

1. Knoester, J. & Mukamel, S. Transient gratings, four-wave mixing and polariton effects in nonlinear optics. *Phys. Rep.* **205**, 1–58. https://doi.org/10.1016/0370-1573(91)90051-M (1991).
2. Eichler, H. J., Günter, P. & Pohl, D. W. *Laser-Induced Dynamic Gratings* (Springer, 1986).
3. Goodno, G. D., Dadusc, G. & Miller, R. J. D. Ultrafast heterodyne-detected transient-grating spectroscopy using diffractive optics. *J. Opt. Soc. Am. B* **15**, 1791–1794. https://doi.org/10.1364/JOSAB.15.001791 (1998).
4. Toscano, J. P., Platz, M. S., Nikolaev, V., Cao, Y. & Zimmt, M. B. The lifetime of formylcarbene determined by transient absorption and transient grating spectroscopy. *J. Am. Chem. Soc.* **118**, 3527–3528. https://doi.org/10.1021/ja953810x (1996).

5. Choi, J., Yang, C., Kim, J. & Ihee, H. Protein folding dynamics of cytochrome c seen by transient grating and transient absorption spectroscopies. *J. Phys. Chem. B* **115**, 3127–3135. https://doi.org/10.1021/jp106588d (2011).
6. Chen, K., Gallaher, J. K., Barker, A. J. & Hodgkiss, J. M. Transient grating photoluminescence spectroscopy: An ultrafast method of gating broadband spectra. *J. Phys. Chem. Lett.* **5**, 1732–1737. https://doi.org/10.1021/jz5006362 (2014).
7. Ghosh, S. et al. Femtosecond heterodyne transient grating studies of nonradiative deactivation of the s2 (11bu+) state of peridinin: Detection and spectroscopic assignment of an intermediate in the decay pathway. *J. Phys. Chem. B* **120**, 3601–3614. https://doi.org/10.1021/acs.jpcb.5b12753 (2016).
8. Hofmann, F., Short, M. P. & Dennett, C. A. Transient grating spectroscopy: An ultrarapid, nondestructive materials evaluation technique. *MRS Bull.* **44**, 392–402. https://doi.org/10.1557/mrs.2019.104 (2019).
9. Lincoln, C. N. et al. A quantitative study of coherent vibrational dynamics probed by heterodyned transient grating spectroscopy. *Vib. Spectrosc.* **85**, 167–174. https://doi.org/10.1016/j.vibspec.2016.04.018 (2016).
10. Choudhry, U. et al. Characterizing microscale energy transport in materials with transient grating spectroscopy. *J. Appl. Phys.* **130**, 231101. https://doi.org/10.1063/5.0068915 (2021).
11. Mairesse, Y. et al. High-order harmonic transient grating spectroscopy in a molecular jet. *Phys. Rev. Lett.* **100**, 143903. https://doi.org/10.1103/PhysRevLett.100.143903 (2008).
12. Janusonis, J. et al. Transient grating spectroscopy in magnetic thin films: Simultaneous detection of elastic and magnetic dynamics. *Sci. Rep.* **6**, 29143. https://doi.org/10.1038/srep29143 (2016).
13. Fourkas, J. T., Brewer, T. R., Kim, H. & Fayer, M. D. Picosecond polarization-selective transient grating experiments in sodium?seeded flames. *J. Chem. Phys.* **95**, 5775–5784. https://doi.org/10.1063/1.461599 (1991).
14. Rouxel, J. R. et al. X-ray circular dichroism measured by cross-polarization X-ray transient grating. *J. Phys. B* **57**, 62. https://doi.org/10.1088/1361-6455/ad6b62 (2024).
15. Weninger, C. et al. Stimulated electronic X-ray raman scattering. *Phys. Rev. Lett.* **111**, 233902. https://doi.org/10.1103/PhysRevLett.111.233902 (2013).
16. Marinelli, A. et al. Tunable X-ray free electron laser multi-pulses with polarization control. *Sci. Rep.* **12**, 1–10. https://doi.org/10.1038/s41598-022-06754-y (2022).
17. Marinelli, A. et al. Terawatt-scale attosecond X-ray pulses from a cascaded free-electron laser. *Nat. Photonics* **18**, 123–128. https://doi.org/10.1038/s41566-024-01427-w (2024).
18. Bencivenga, F. et al. Nanoscale transient gratings excited and probed by extreme ultraviolet femtosecond pulses. *Sci. Adv.* **5**, 5805. https://doi.org/10.1126/sciadv.aaw5805 (2019).
19. Bencivenga, F. et al. Experimental setups for fel-based four-wave mixing experiments at fermi. *J. Synchrotron Radiat.* **23**, 132–140. https://doi.org/10.1107/S1600577515021104 (2016).
20. Foglia, L. et al. Nanoscale polarization transient gratings. *Nat. Commun.* **14**, 54799. https://doi.org/10.1038/s41467-024-54799-6 (2023).
21. Yao, K. et al. All-optical switching on the nanometer scale excited and probed with femtosecond extreme ultraviolet pulses. *Phys. Rev. Lett.* **128**, 087401. https://doi.org/10.1103/PhysRevLett.128.087401 (2022).
22. Masciovecchio, C. et al. EIS: the scattering beamline at FERMI. *J. Synchrotron Radiat.* **22**, 553–564. https://doi.org/10.1107/S1600577515003380 (2015).
23. Kubec, A. et al. An achromatic X-ray lens. *Nat. Commun.* **13**, 1305. https://doi.org/10.1038/s41467-022-28902-8 (2022).
24. Flenner, S. et al. Hard X-ray nano-holotomography with a fresnel zone plate. *Opt. Express* **28**, 37514–37525. https://doi.org/10.1364/OE.411616 (2020).
25. Katayama, K., Sato, K., Sugiya, H. & Shoji, T. Near-field heterodyne transient grating spectroscopy. *Chem. Phys. Lett.* **479**, 306–309. https://doi.org/10.1016/j.cplett.2009.08.025 (2009).
26. Svetina, C. et al. Towards X-ray transient grating spectroscopy. *Opt. Lett.* **44**, 574–577. https://doi.org/10.1364/OL.44.000574 (2019).
27. Rouxel, J. R. et al. Hard X-ray transient grating spectroscopy on bismuth germanate. *Nat. Photonics* **15**, 499–503. https://doi.org/10.1038/s41566-021-00797-9 (2021).
28. Morillo-Candas, A. S. et al. Time resolved hard X-ray/optical transient grating spectroscopy on a liquid jet. In *Conference on Lasers and Electro-Optics/Europe (CLEO/Europe 2023) and European Quantum Electronics Conference (EQEC 2023), Technical Digest Series* (Optica Publishing Group, 2023).
29. Ferrari, E. et al. All hard X-ray transient grating spectroscopy. https://doi.org/10.21203/rs.3.rs-4819983/v2 (2024).
30. Talbot, H. F. Facts relating to optical science. *Philos. Mag. Ser.* **3**(9), 401–407 (1836).
31. Hagen, N., Kupinski, M. & Dereniak, E. L. Gaussian profile estimation in one dimension. *Appl. Opt.* **46**, 5374–5383. https://doi.org/10.1364/AO.46.005374 (2007).
32. Saghafi, S. & Sheppard, C. J. R. Near field and far field of elegant hermite-gaussian and laguerre-gaussian modes. *J. Mod. Opt.* **45**, 1999–2009. https://doi.org/10.1080/09500349808231738 (1998).
33. Podanchuk, D. V. et al. Influence of aperture size on wavefront sensor based on the Talbot effect. *Proc. SPIE* **9066**, 90660S (2013).
34. Podanchuk, D., Goloborodko, A., Kotov, M. & Petriv, D. Talbot sensor with diffraction grating adaptation to wavefront aberrations. *Ukr. J. Phys.* **60**, 10–14. https://doi.org/10.15407/ujpe60.01.0010 (2015).
35. Goodman, J. *Introduction to Fourier Optics. Chapter 4. Fresnel and Fraunhofer Diffraction. McGraw-Hill Physical and Quantum Electronics Series* (Roberts & Company, 2005).
36. Cheng, J., Zhou, J. & Yan, Y. Theory of pump-probe propagation in third-and higher-order, nonlinear optical media. *J. Opt. Soc. Am. B* **21**, 364–369. https://doi.org/10.1364/JOSAB.21.000364 (2004).
37. Guo, J., Wang, H., Dai, X., Xiang, Y. & Tang, D. Enhanced nonlinear optical responses of graphene in multi-frequency topological edge modes. *Opt. Express* **27**, 32746–32763. https://doi.org/10.1364/OE.27.032746 (2019).
38. Goldman, S. *Frequency Analysis Modulation and Noise, Radio Communication Series* (McGraw-Hill, 1948).
39. He, L. & Feng, B. *Fundamentals of Measurement and Signal Analysis* (Springer, 2022).
40. Francon, M. *Laser Speckle and Applications in Optics* (Elsevier, 2012).
41. Almeida, J. M. P., Gomes, A. S. L., Loures, K. H., de Araújo, C. B. & de Matos, S. J. M. Wavelength dependence of the nonlinear refractive index and two-photon absorption coefficient in diamond. *Sci. Rep.* **7**, 14320. https://doi.org/10.1038/s41598-017-14748-4 (2017).
42. Tamasaku, K. et al. X-ray two-photon absorption competing against single and sequential multiphoton processes. *Nat. Photonics* **8**, 313–316. https://doi.org/10.1038/nphoton.2014.10 (2014).
43. Buathong, S., Srisuphaphon, S. & Deachapunya, S. Probing vortex beams based on talbot effect with two overlapping gratings. *J. Opt.* **24**, 025602. https://doi.org/10.1088/2040-8986/ac477c (2022).
44. Kotov, M., Danko, V. & Goloborodko, A. Talbot wavefront sensor measurement possibilities under Gaussian illumination. *J. Opt. Soc. Am. A* **40**, 444350. https://doi.org/10.1364/JOSAA.444350 (2023).
45. Weitkamp, T., David, C., Kottler, C., Bunk, O. & Pfeiffer, F. Tomography with grating interferometers at low-brilliance sources. In *Developments in X-ray Tomography V, vol. 6318 of Proceedings of SPIE, 63180S*, (Bonse, U. ed.) https://doi.org/10.1117/12.683851. International Society for Optics and Photonics (SPIE, 2006).
46. Goloborodko, A. Talbot phenomenon in binary optical gratings under Gaussian illumination. *Optik* **312**, 171973. https://doi.org/10.1016/j.ijleo.2024.171973 (2024).

47. Kotov, M. & Goloborodko, A. Performance of a reference-free wavefront sensor based on the Talbot effect under Gaussian illumination. *J. Opt. Soc. Am. A* **41**, C22–C27. https://doi.org/10.1364/JOSAA.527337 (2024).
48. Podanchuk, D. V. et al. Adaptive wavefront sensor based on the Talbot phenomenon. *Appl. Opt.* **55**, B150–B157. https://doi.org/10.1364/AO.55.00B150 (2016).
49. Goloborodko, A. Wavefront curvature restoration by a sensor based on the talbot phenomenon under gaussian illumination. *J. Opt. Soc. Am. A* **40**, B8–B14. https://doi.org/10.1364/JOSAA.476871 (2023).
50. Shi, X., Yang, W., Xing, H. & Chen, X. Discrete plasmonic talbot effect in finite metal waveguide arrays. *Opt. Lett.* **40**, 1635–1638. https://doi.org/10.1364/OL.40.001635 (2015).
51. Afshari-Bavil, M. et al. The observation of plasmonic Talbot effect at non-illumination side of groove arrays. *Plasmonics* **13**, 2387–2394. https://doi.org/10.1007/s11468-018-0765-8 (2018).
52. Kotov, M. M. & Goloborodko, A. A. Measurement range of Talbot wavefront sensor. *Opt. Eng.* **56**, 014101. https://doi.org/10.1117/1.OE.56.1.014101 (2017).
53. Born, M. & Wolf, E. (eds.) *Principles of Optics. Chapter 8. Elements of the Theory of Diffraction*. (Cambridge University, 2001).
54. Maznev, A. A., Nelson, K. A. & Rogers, J. A. Optical heterodyne detection of laser-induced gratings. *Opt. Lett.* **23**, 1319–1321. https://doi.org/10.1364/OL.23.001319 (1998).

Acknowledgements

CS and CSe acknowledge funding from the Spanish Ministry of Science, Innovation and Universities through project PID2023-152154NB-C21. CS also acknowledges funding from the "Severo Ochoa" Programme for Centres of Excellence in R&D (CEX2020-001039-S/AEI/10.13039/501100011033).

Author contributions

CS envisioned the need for this theoretical study. AG and CSe developed the theoretical framework, implemented the code and conducted and analyzed the simulations. All authors collaboratively contributed to writing the manuscript.

Funding

CS and CSe acknowledge funding from the Spanish Ministry of Science, Innovation and Universities through project PID2023-152154NB-C21. CS also acknowledges funding from the "Severo Ochoa" Programme for Centres of Excellence in R&D (CEX2020-001039-S/AEI/10.13039/501100011033).

Declarations

Competing interests

The authors declare no competing interests.

Additional information

Correspondence and requests for materials should be addressed to C.S.

Reprints and permissions information is available at www.nature.com/reprints.

Publisher's note Springer Nature remains neutral with regard to jurisdictional claims in published maps and institutional affiliations.